Sub-100 Nanometer Ion Beam Probe for Biological and Other Applications

S. K. Guharay[1], V. Jabotinski[1], J. Orloff[2]

[1]FM Technologies, Inc., 4431-H Brookfield Corporate Dr., Chantilly, VA 20151; [2]Institute for Research in Electronics and Applied Physics, University of Maryland, College Park, MD 20742.

Focused ion beams, at sub-100 nanometer scale, have utility for many important applications in both basic and applied science. The critical issues to achieve a high-resolution ion beam probe with target beam intensity of about 1 A/cm^2 are governed by beam characteristics from the ion source, namely, virtual source size, beam brightness, and energy spread. The state-of-the art of sources needs to be advanced so that desirable beam characteristics for a variety of beam species, especially, for hydrogen, oxygen, argon, and many complex molecular ions, can be achieved. This article focuses on developing high-brightness negative ion beams and coupling the beams to an ion-optical column with the goal to achieve a sub-100 nm ion beam probe. Negative ion beams have unique merits in applications involving beam-material interactions: (a) surface charging voltage for an electrically isolated surface does not exceed a few volts, and (b) charging voltage is almost independent of the beam energy. These properties can be utilized to avoid undesirable surface charging that often result in device or sample damage and ion-beam defocusing. Experimental results on ion beam characteristics, key results of ion-optical calculations to achieve sub-100nm beam spot and examples showing merits of negative ion beams are described.

I. INTRODUCTION

Focused ion beams (FIB) at sub-100 nanometer scale have utility for a variety of applications in biology, microelectronics, materials research, geology and space science. The role of ion beam analysis in biology and medicine was reviewed earlier [Maenhaut, 1988]. It has been noted that ion microscopy's high sensitivity makes it an ideal tool for localizing anticancer drugs inside tumor cells [Chandra, 2000; Chandra and Lorey, 2001]. An immensely useful imaging methodology would be one that is sensitive enough to give an accurate measure of the minute quantities of material in cells as well as possess the spatial resolution to distinguish organelles. Imaging by FIB-SIMS (Secondary Ion Mass Spectrometry) seems very attractive in these applications. Mapping distributions of targeted chemical species in cells with about 10-nm resolution will allow investigation of many fundamental problems in cell biology relevant to studies of carcinogenesis, toxicology, and neurochemistry as well as the diagnosis of several diseases including cancer. In addition to mapping the fine-scale distribution of targeted chemical species in cancer cells, high-resolution ion beam probes have applications in a broad range of disciplines in science and technology including many other areas in biology, medicine and nanotechnology overall. Some examples relevant to semiconductor manufacturing are ion beam milling and diagnostic instruments including in-line inspection of semiconductor devices for defect management. Furthermore, a high sensitivity analytical technique can be developed using ion beam probes to satisfy the needs for Homeland Security for detecting traces (less than part per billion) of very low vapor pressure explosives.

While ion beams have been very widely used for many applications, especially in microelectronics, their importance in biology and medicine has been recognized only recently. There has been spectacular growth in this area both from the standpoint of basic research and applications. A

group in Université Paris-Sud [Slodzian, 1987; Castaing and Slodzian, 1962; http://www.curie.u-psud.fr/U350/SIMS.html] has been pursuing SIMS analysis to probe a wide range of problems in biology, namely, (a) Antitumor pharmacology: Intracellular localization of new antitumor drugs, Intracellular traffic of plasmidic DNA designed for gene therapy, Intracellular localization of antisens oligonucleotides; (b) Cytogenetic studies of cancer cells: Analysis of the distribution of Mg, Ca and Zn ions and of Br, F and I atoms in metaphasic chromosomes; and (c) Nuclear medicine and radiotoxicology: Applications in diagnosis and treatment of melanoma. Recent interests of the Surface and Microanalysis Science Division at the National Institute of Standards and Technology (NIST) include problems of localization and imaging of trace element distributions in human brain neurons by SIMS [Gillen et al., 1994; Smith et al., 1994]. A group at Harvard has been actively engaged in novel SIMS development for biological research [Guillermier et al., 2003; Hallegot et al., 2004].

Two major components of an overall FIB unit are an ion source and a focusing ion-optical column. Considering the needs for FIB-SIMS instrumentation, an improved primary ion beam probe is a basic major requirement to advance the overall technology. The fundamental technical constraints can be recognized from the recent results obtained with NanoSIMS50 – this is one of the most powerful high-resolution SIMS apparatus developed by CAMECA, a French company [http://www.cameca.fr/doc_en_pdf/ns50_biology_application_booklet_july2004_a4p_web.pdf; http://www.cameca.fr/doc_en_pdf/ns50_instrumentation_booklet_july2004_a4p_web.pdf.]. A spot size of the order of hundreds of nanometers at the current of about 2-3 picoampere for O^- beams was noted. The major limitation appears to be due to the duoplasmatron sources used for producing the primary ion beam. Such sources cannot provide high-quality O^- beams. At least an order of magnitude improvement in the beam brightness from the current level of $10A/(cm^2sr)$,

and an appropriately matched ion-optical column, is the primary challenge for a high-resolution O^- SIMS machine.

This article focuses on developing high-brightness negative ion beams and coupling the beams to an ion-optical column. The goal is to achieve a sub-100 nm ion beam probe and apply it to suit the needs for the aforementioned applications. Negative ions have unique merits for the aforementioned applications involving beam-materials interactions. When negative ions strike a surface, especially an electrically isolated surface, the surface charging voltage does not exceed a few volts, and it is almost independent of the beam energy [Ishikawa, 1996; Guzdar et al., 1997]. This advantage can be utilized to avoid device or sample damage, ion-beam defocusing, and other deleterious effects.

Measurements of ion-beam characteristics, beam-materials interactions showing self-regulation of the surface charging voltage as well as a novel scheme for removing organic contamination, and key results pertaining to ion-optical calculations to achieve a sub-100 nm focused spot are described in the following sections.

II. RESULTS

A. Negative Ion Beam Characteristics

A negative ion beam test stand facility, equipped with a large number of beam diagnostics, has been developed. The compact negative ion source has a Penning-type geometry of the electrodes. The discharge cell has a volume of about 0.25 cm^3. The desired species of gas, such as hydrogen, oxygen, argon, is injected into the cell via a gas valve and a discharge is produced. As described earlier [Guharay et al., 1996; Guharay et al., 1998; Guharay et al., 1999] cesium vapor is injected into the cell from an oven to catalyze negative ion production. The important parameters determining the source operating conditions are gas pressure, discharge voltage, cesium vapor pres-

sure, and beam extraction voltage. Upon completing detailed studies of this source in pulsed mode of operation, we have successfully achieved stable dc operation.

In pulsed mode, we achieved an O^- angular beam intensity of greater than 20 mA/sr for discharge current density of about 38 A/cm^2. Similar beam intensity was measured for H^- beams; however, the extraction gap was appropriately adjusted taking into account the beam species and applied extraction voltage which satisfies the space-charge limited emission condition. The source also produced intense positive ion beams, including Ar^+ ion beams, and the beam intensity was close to that of the above negative ion beams [Guharay et al., 1999].

We have noted that the emission current density j_e of the negative ion beam scales almost linearly with the discharge current density j_d, and the slope of the j_e versus j_d curve is $\lesssim$0.02. As stated later, this relationship was found to remain almost independent of the duty factor of the source operation. The key results of our recent experiments in dc mode and characteristic beam parameters are presented below.

In order to prevent the ion source from overheating in dc operation the discharge current was maintained at a level close to the average discharge current in pulsed operation. Accordingly, the average discharge power $<P_d>$ responsible for heating the source did not change. Therefore, the source temperature did not exceed the limits that the cooling system can handle. The source was operated in dc mode with the discharge current ranging over 0.1-1.5 A. The tests resulted in stable, sustainable, low noise, fully controllable discharge.

Figure 1 shows the noiseless dc discharge current of 1.5A at a voltage across the discharge gap of 100V. The signal-to-noise ratio for the H^- beam, Fig.2, is close to 11. A much more intense and “noiseless” beam is expected with an upgraded vacuum system.

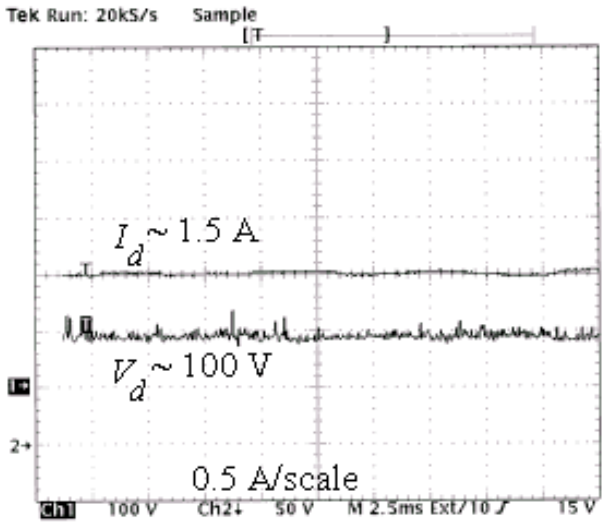

Figure 1 "Noiseless" discharge in dc mode; I_d = 1.5 A

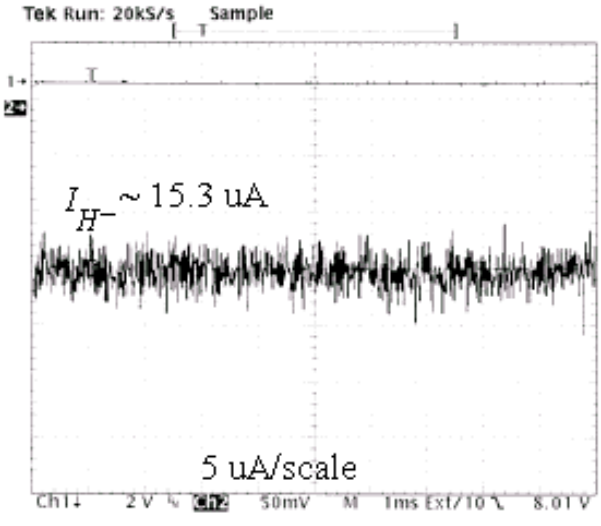

Figure 2 Typical oscilloscope trace of a dc H^- beam; I_{H^-} = 15.3 μA through an emission aperture of diameter = 0.35 mm for I_d = 1.5 A.

The results of some characteristic parameters for preliminary dc operation of the source are summarized: discharge current, I_d =1.5 A; discharge voltage, V_d = 100 V ; average discharge power, $\langle P_d \rangle = \langle V_d I_d \rangle$ = 150 W; H^- beam current, I_{H^-} =15.3 μA through an emission aperture of diameter d_0 =0.35 mm, and source temperature = 677 K

It has been noted that the basic discharge parameters and properties of H^- beams did not deteriorate while switching the operation from pulsed to dc mode. We had earlier measured the unnormalized brightness of 10^5 A/(cm^{2}sr) and the energy spread of $\lesssim$ 3 eV for pulsed H^- beams [Guharay et al., 1998].

B. Surface Charging due to Negative Ion Beam Irradiation

We measured the charge-up voltage when H^- beams struck the surfaces of electrically isolated materials including n-type doped silicon, aluminum, and alumina. Figure 3 shows the results of the conductor charge up experiments. A maximum charge-up voltage of 1.5 V was observed for beam energy of 5 keV H^- beam. For silicon, the peak charge up voltage occurred at the beam en-

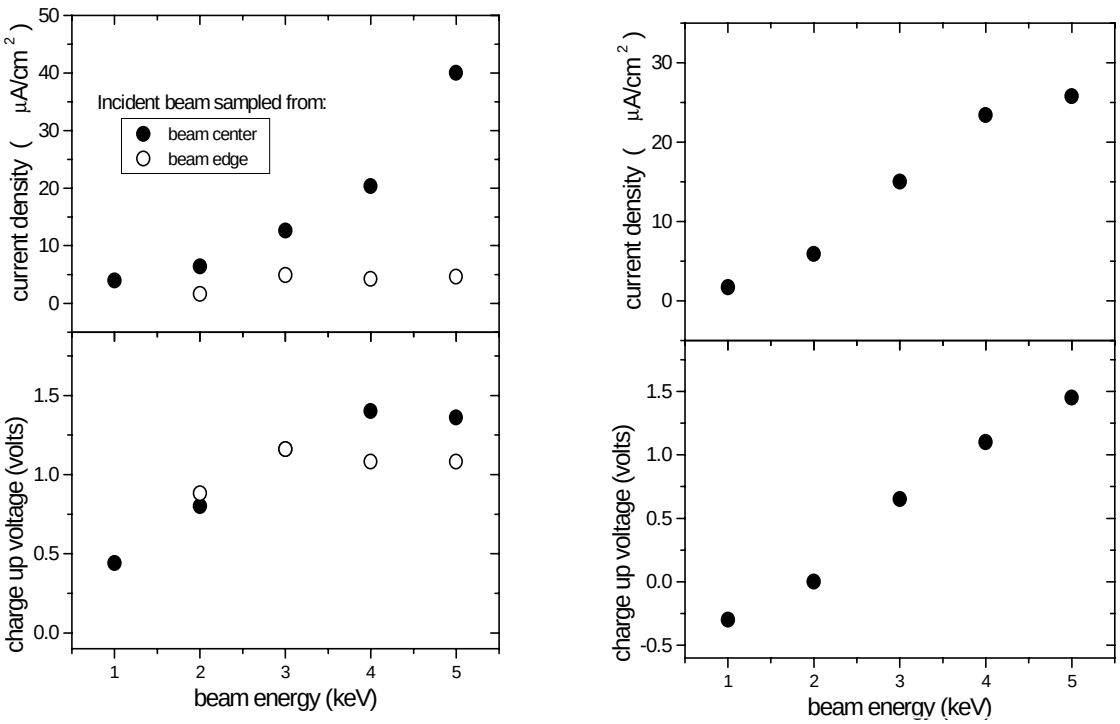

Figure 3: The charge up voltage of silicon (left) and aluminum (right) vs. beam energy. Solid circles represent measurements for higher current densities and open circles for lower current densities. The charge up voltage was not sensitive to the variation of the beam current density.

ergy of 4-5 keV, but for aluminum, the charge up shows an increasing trend. Higher current density causes a small increase in the charge-up voltage. This is evident at higher beam energies.

Figure 4 shows the charge-up voltage of an insulator, alumina, as a function of the beam energy. The charge-up voltage is observed to clamp at about 3V and insensitive to the variation in the beam energy.

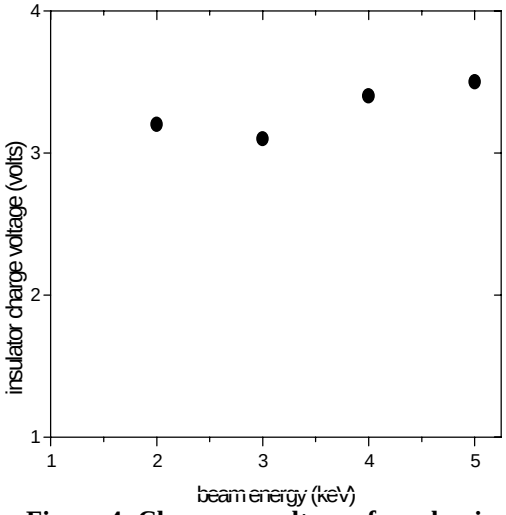

Figure 4: Charge up voltage of an alumina disc as a function of H^- beam energy.

C. Removal of Hydrocarbon Contaminants using Negative Ion Beam Treatment

(i) Contamination due to pump oil

The common sources for hydrocarbon-based contaminations in an industrial environment, including semiconductor manufacturing, are contaminations from pump oil,

human body oil, etc. Therefore, a case study with pump oil was conducted. A part of a wafer sample was coated with a thin layer of HE 500 pump oil. XPS (X-ray Photoelectron Spectroscopy) spectra were analyzed when the results for a contaminated and unirradiated site was compared to its neighboring contaminated site after H^- beam irradiation. A summary of the results for C and Si abundances (in atomic %) at unirradiated and irradiated sites with initial uniform oil contamination at all sites is shown in Fig.5. In all ion-beam irradiated sites, the C-level dropped significantly, above 50%, compared to its value in neighboring unirradiated sites, and the Si-level correspondingly enhanced to a level close to a bare substrate's composition. The C and Si-levels in ion-beam treated sites reached almost the level of a fresh substrate after its residence in the experimental environment. This clearly demonstrates the effectiveness of the processing method for hydrocarbon removal. An estimated removal rate of ~1.7 cubic micrometer of HE-500 pump oil contamination per microcoulomb of H^- at ~5keV was obtained. This experiment was conducted with the source in pulsed mode of operation at a duty factor of 0.006, and the removal rate was ~15Å/hr. In dc mode, this rate will be enhanced by three to four orders of magnitude.

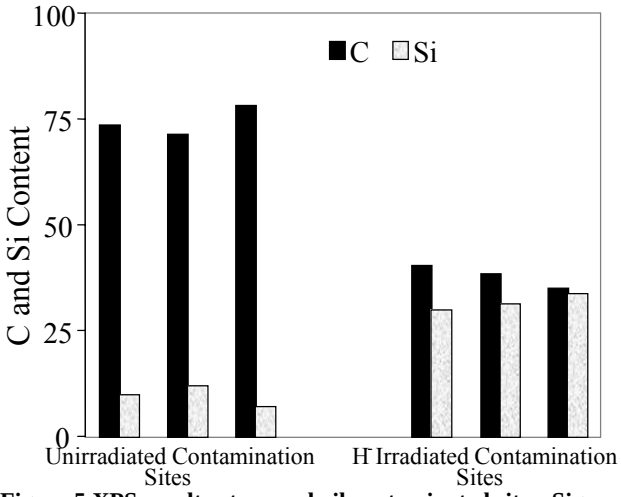

Figure 5 XPS results at several oil contaminated sites. Significant reduction of carbon is noted at all sites irradiated by ion beams. Here the carbon levels are reduced to approximately those for background samples.

(ii) Removal of PMMA resists on wafers

The surface of silicon sample wafers was spin-coated with 1-μm thick PMMA (PolyMethyl MethAcrylate, $C_5H_8O_2$) resists. H^- beams of 5 keV irradiated the wafers at three dosages,

namely, $5x10^{15}$, 10^{16}, and $5x10^{16}$ ions/cm^2. The surface flatness was examined using an Alpha-Step 500 Profilometer. Resist materials were removed in all three beam irradiated places since the profilometer measured a clean step into the resist thickness from the top surface. The depth

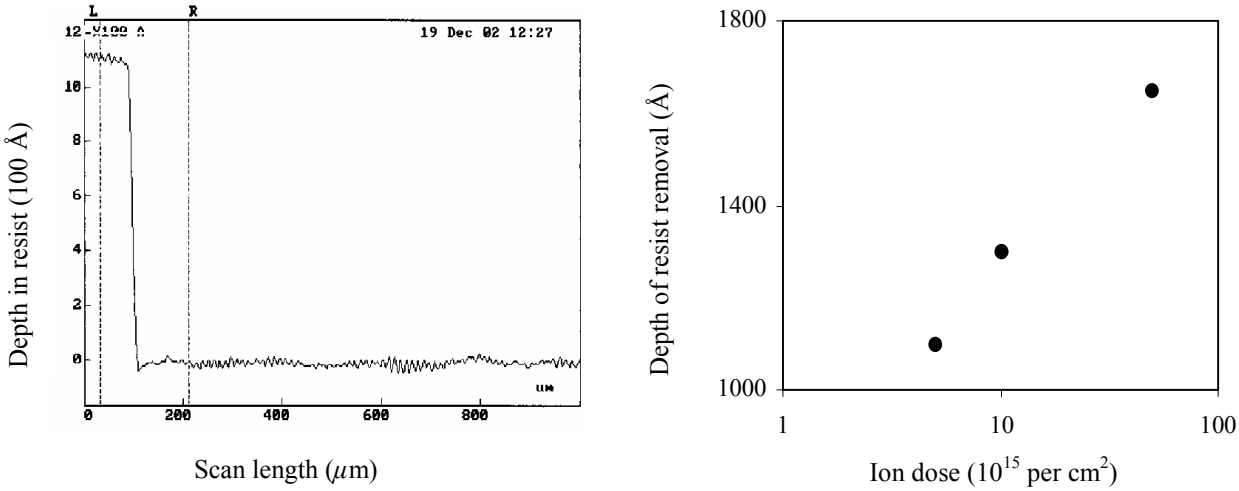

Figure 6: Left figure -- Typical Profilometer scan of PMMA resist coated wafer surface after ion beam irradiation. Horizontal scale in μm shows scan length over ~ 1mm and the vertical scale in Å (x100) shows the depth of resist removal. Dose ~5x10^{15} ions/cm^2. A clear step down into the resist is visible indicating resist removal. Right figure -- Resist removal versus ion beam dosage. Horizontal scale has log-scale.

of resist removal in the beam-irradiated region varied from ~ 1100 to 1700Å as the H^- dose changed from $5x10^{15}$, 10^{16}, and $5x10^{16}$ ions/cm^2. The results for a typical profilometer scan covering the irradiated regions are shown in Fig.6 (left), and the depth of resist removal vs. H^- dose is shown in the right figure. The results are plotted in a semi-log scale, and the trend follows similar behavior as previously reported for etching of PMMA resists by focused Ar beams [Harakawa and Yasuoka, 1987; Valiev, 1992]. The PMMA removal rate was observed to be ~ 2 μm^3/nC of H^- at ~5keV. The removal rate was 170Å/hr. Note that this value was obtained in the pulsed mode with a duty factor of 0.006. These results with H^- beams can be compared with previously reported PMMA resist removal rate of 85 to 106 Å/hr by oxygen/RF discharge [www.sematech.org/public/resources/litho/euvl/euvl2000/documents/202_ENV02_graham.pdf].

D. Ion-Optical Column for sub-100nm Ion Beam Probe

To design a charged particle optical system we started from the requirements imposed by the intended use of that system – source properties, beam spot FWHM or 15-85% rise distance, allowable current density distribution shape, current, beam energy, working distance etc.

We have calculated the theoretical performance of a three-lens column using what are believed to be conservative parameters for the O^- source in dc operation: angular intensity $J_\Omega = 5$ mA sr^{-1}, and virtual source size (based on the source emittance) of 20 μm (FWHM). The focusing lenses consist of two condenser lenses providing a total of 100X demagnification followed by an objective lens with 5 mm working distance, providing 10X demagnification. The performance was calculated by looking at the properties of the final lens as a function of beam current, which determines the aperture angle in the exit pupil of the objective lens.

The calculations were done assuming a Gaussian current distribution with a FWHM of 200 nm at the crossover of the second condenser lens; this is the object that the objective lens images onto the target. The computer code used [Orloff, et al., 1991] calculated the current distribution J(r) generated by the final lens taking into account the current distribution of the crossover and the chromatic and spherical aberration of the final lens. The calculations were performed at various points on the optical axis relative to the Gaussian focal plane, Z_G, that is with a defocus which can be positive (downstream from Z_G) or negative (upstream from Z_G). In addition, the current distribution J(r) was integrated. This allowed simulation of the focused beam passing across a knife edge to determine the rise-distance of the current. This is an extremely useful function, since when the relatively large currents are needed the optical system will be limited by the spherical aberration (C_s), and the effect on the beam properties is quite pronounced (see below).

We calculated the beam rise-distances for the currents of 1, 2, 5, and 10 pA as shown in Fig. 7.

We used a telecentric deflection system to allow beam rastering over an area of about 10 μm^2. A peak voltage of a few tens of volts with a repetition rate of a few kilohertz will provide the required beam rastering. The significance of the rise-distance, which is the distance for the beam current intercepted by a knife edge to increase from 15 to 85% of its full value (typically), is that this represents the effect of spherical aberration very strongly. That is, at a low current and small aperture angle, where the beam size is determined almost entirely by the demagnification of the optical system (ignoring space charge effects), the rise-distance will be close to the FWHM of J(r). At high currents and large aperture angles, the rise distance can be orders of magnitude larger than the FWHM of J(r). This is because a large amount of the beam current is contained in

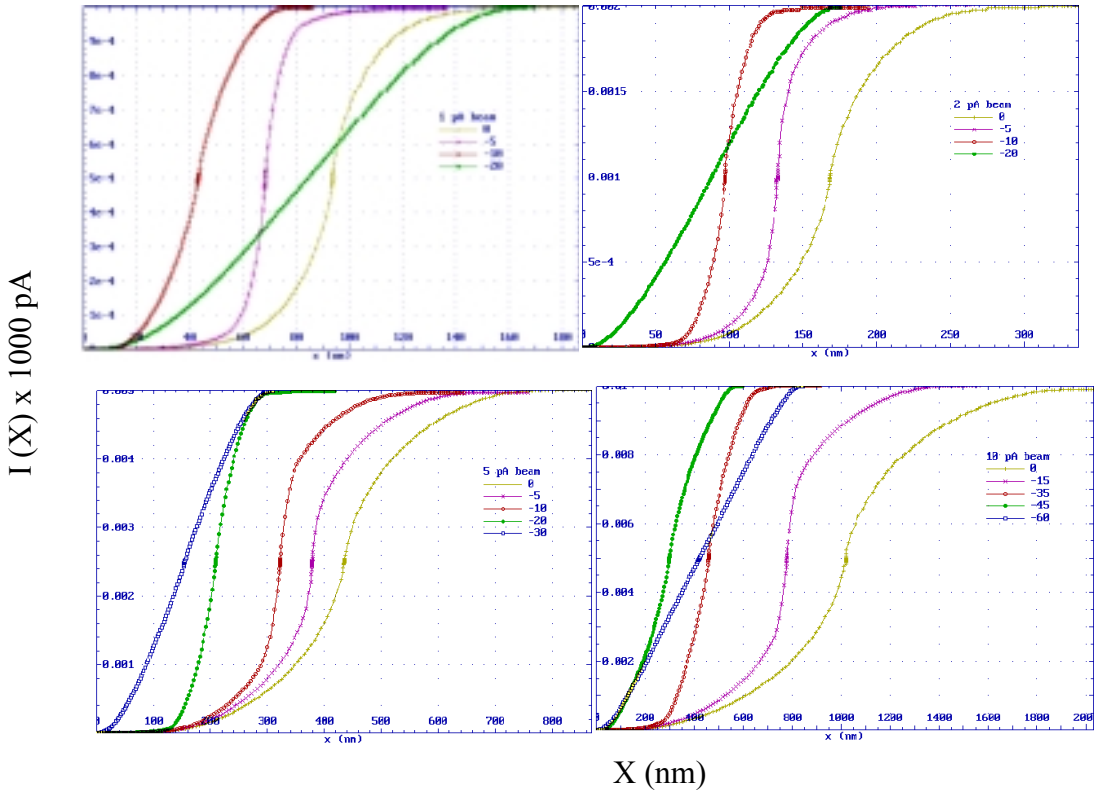

Figure 7 Results for working distance of 5 mm. Rise distance as a function of defocus for O^- beam currents of 1 pA (top left), 2 pA (top right), 5 pA (bottom left) and 10 pA (bottom right). The best rise distances are: about 13 nm at -5 micrometer defocus for 1 pA; about 40 nm at -10 micrometer defocus for 2 pA; about 100 nm at -20 micrometer defocus for 5 pA; and about 300 nm at -35 micrometer defocus for 10 pA. Inset in each figure shows the defocus distance in micrometer relative to the Gaussian plane location Z_G. The rightmost curve in each case corresponds to $Z_G = 0$, i.e. at Gaussian focal plane.

the tails of the current density distribution. Even though the current density far from the beam axis may be small, the current carried in the beam tails can be significant because of the large distances involved (equal to $C_{si} \sim \alpha^{3}$).

The rise-distance appears a better measure of the performance of a SIMS system than the FWHM of the current distribution (which essentially determines the imaging resolution of the system), since a SIMS signal will be generated everywhere the beam strikes and it may not be easy to disentangle this signal from that produced under the core of the focused beam. This is unlike the situation in ordinary imaging where the beam tails mainly cause a loss of contrast, which may not prevent critical details from being resolved.

The results in Fig. 7 were obtained for a working distance of 5 mm. It is important to examine the effect of working distance. For high-resolution SIMS, the working distance is kept extremely small – CAMECA's nano-SIMS instrument uses a working distance of about 500 μm [http://www.cameca.fr/doc_en_pdf/ns50_instrumentation_booklet_july2004_a4p_web.pdf].

As shown in Fig. 8, a significant improvement in spatial resolution of the beams is noted by reducing the working distance. For example, the 15-85% rise distance is about 70 nm versus the

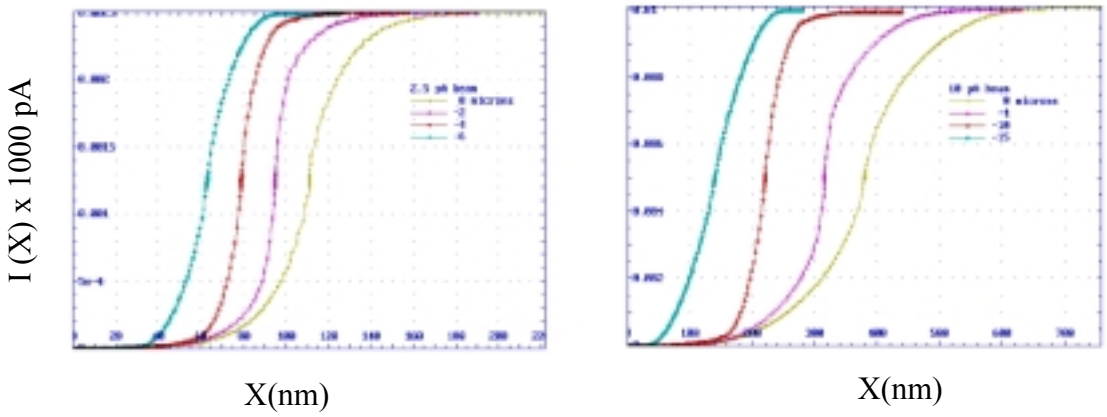

Figure 8: Rise distance for working distance of 0.5 mm. Left: 2.5 pA O^- beam -- best rise distance is about 20 nm at –4 micrometers defocus. Right: 10 pA O^- beam -- best rise distance is about 70 nm at – 10 micrometer defocus

earlier value of 300 nm for a working distance of 5 mm for beam current as high as 10 pA. Note that the rise distance is as low as 20 nm at a working distance of 0.5 mm and it increases to 60 nm for working distance of 5 mm.

The above design analysis presents values of spatial resolution and beam current density at the target that exceed the present state-of-the art by about two orders of magnitude. A conventional duoplasmatron source, when coupled with the excellent optics of CAMECA's nano-SIMS system [http://www.cameca.fr/doc_en_pdf/ns50_instrumentation_booklet_july2004_a4p_web.pdf], can only achieve a 170 nm rise-distance with 0.3 pA current, and at the 2 pA current the rise distance increases by two times to 340 nm.

Figure 9 shows an example of H^- beam spot when the beam from the source was focused using a simple einzel lens with magnification of about 0.1. The beam distribution at the focused spot (left figure in Fig.9) was obtained by exposing PMMA resists for different beam dwell times and then examining the resist exposures using a scanning electron microscope. This spot size of about 2 μm (right photograph in Fig. 9) achieved by using a lens magnification of about 0.1 suggests that a focused spot size of about 20 nm is achievable by an additional magnification of 0.01. This establishes the merit of the ion-optical system discussed earlier in this section.

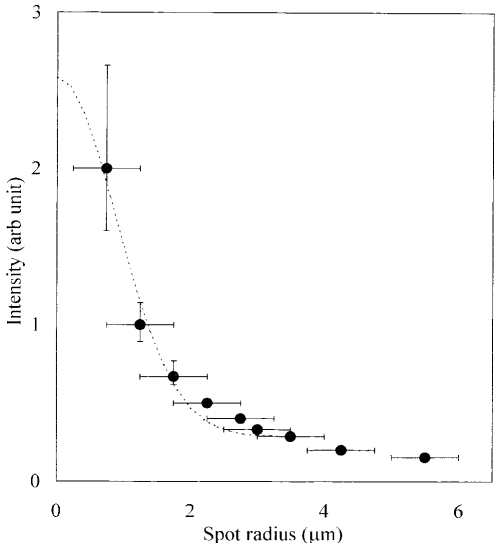

2 μm

Figure 9: Right photograph -- SEM picture of a focused beam spot. Left figure --- beam intensity distribution at the focused spot. This yields a spot size of about 2 micrometer.

Discussions and Conclusions

This article describes the development of a sub-100 nm level ion beam probe for various critical applications including biology. The thrust of this work lies on developing a dc ion source that can deliver high-brightness and low energy spread negative ion beams. Additionally, the beam from the source is coupled to an appropriate ion-optical column that can focus it to a sub-100 nm scale spot size. Measured beam characteristics, preliminary beam focusing results and the design of an ion-optical column demonstrate the feasibility of achieving a sub-100 nm ion beam probe. Unique merits of the negative ion beams in mitigating surface charge-up problem as well as cleaning of surface contaminations, especially due to hydrocarbons in the environment, have been demonstrated.

This new ion beam probe can be utilized to build a high-resolution FIB-SIMS system for studying many critical problems in biology. Over and above, high-brightness ion beam probes have demands in many applications for semiconductor industries, such as ion beam milling and analytical instrumentation for studying defects in semiconductor devices. A powerful tool for in-line defect management can be designed using this negative ion-beam based analytical technique.

Acknowledgments

This work is supported by SBIR Grants from National Cancer Institute and National Institute of Biomedical Imaging and Bioengineering of National Institute of Health. The first author (SKG) acknowledges helpful discussions with Professors K. Baidoo and H. Wagner of The Johns Hopkins University Bloomberg School of Public Health and Dr. G. Derevyankin of The Budker Institute of Nuclear Physics, Novosibirsk, Russia. The role of Dr. S. Douglass in measurements of surface charging and beam-surface interactions is gratefully acknowledged.

References

W. Maenhaut (1988) Nucl. Instrum. Meth. in Phys. Res. B35, 388.

S. Chandra (2000) http://www.news.cornell.edu/Chronicles/10.12.00/imaging_drugs.html.

S. Chandra and D. R. Lorey (2001) Cell. Mol. Biol. 47, 503.

G. Slodzian (1987) Optik 77, 148.

R. Castaing and G. Slodzian (1962) J. Microscopy 1, 395.

http://www.curie.u-psud.fr/U350/SIMS.html

G. Gillen, J. Nuygen, C. Sywt, Q. Deng, D.R. Brady and Q. Smith (1994) Secondary Ion Mass Spectrometry, SIMS 9, John Wiley and Sons, Chichester, p. 585.

Q.R. Smith, Q.S. Deng, D.R. Brady, C. Swyt, J. Nguyen and G. Gillen (1994) Proc. Fourth International Conf. on Aluminum and Health.

C. Guillermier, C. P. Lechene, J. Hill, and F. Hillion (2003) Rev. Sci. Instrum. 74, 3312.

P. Hallegot, R. Peteranderl, and C. Lechene (2004) J. Investigative Dermatology 122, 381.

http://www.cameca.fr/doc_en_pdf/ns50_biology_application_booklet_july2004_a4p_web.pdf.

http://www.cameca.fr/doc_en_pdf/ns50_instrumentation_booklet_july2004_a4p_web.pdf.

J. Ishikawa (1996) Rev. Sci. Instrum. 67, 1410.

P. N. Guzdar, A. S. Sharma, and S. K. Guharay (1997) Appl. Phys. Lett. 71, 3302.

S. K. Guharay, W. Wang, V.G. Dudnikov, M. Reiser, J. Orloff, and J. Melngailis (1996) J. Vac. Sci Technol. B14, 3907.

S. K. Guharay, E. Sokolovsky, and J. Orloff (1998) J. Vac. Sci Technol. B16, 3370.

S. K. Guharay, E. Sokolovsky, and J. Orloff (1999) J. Vac. Sci Technol. B17, 2779.

S. K. Guharay, S. Douglass and J. Orloff (2004) Applied Surface Science 231-232, 926.

K. Harakawa, and Y. Yasuoka (1987) J. Vac. Sci. Technol. B4, 355.

Kamil Valiev (1992) The Physics of Submicron Lithography, Plenum Press, N.Y.

www.sematech.org/public/resources/litho/euvl/euvl2000/documents/202_ENV02_graham.pdf

J. Orloff, J-Z. Li and M. Sato (1991) J. Vac. Sci. Tech. B9, 2609.